PCCP

Is Non-Statistical Dissociation a General Feature of Guanine–Cytosine Base-Pair ions? Collision-Induced Dissociation of Protonated 9-Methylguanine–1-Methylcytosine Watson-Crick Base Pair, and Comparison with Its Deprotonated and Radical Cation Analogues

Journal:	*Physical Chemistry Chemical Physics*
Manuscript ID	CP-ART-08-2020-004243.R1
Article Type:	Paper
Date Submitted by the Author:	17-Sep-2020
Complete List of Authors:	Sun, Yan; Queens College of the City University of New York, Chemistry and Biochemistry Moe, May; Queens College of the City University of New York, Chemistry and Biochemistry Liu, Jianbo; Queens College of the City University of New York, Chemistry and Biochemistry

Is Non-Statistical Dissociation a General Feature of Guanine–Cytosine Base-Pair ions? Collision-Induced Dissociation of Protonated 9-Methylguanine–1-Methylcytosine Watson-Crick Base Pair, and Comparison with Its Deprotonated and Radical Cation Analogues

Yan Sun,[ab] May Myat Moe[ab] and Jianbo Liu*[ab]
[a] Department of Chemistry and Biochemistry, Queens College of the City University of New York, 65-30 Kissena Blvd., Queens, NY 11367, USA; [b] Ph.D. Program in Chemistry, The Graduate Center of the City University of New York, 365 5th Ave., New York, NY 10016, USA

Abstract A guided-ion beam tandem mass spectrometric study was performed on collision-induced dissociation (CID) of protonated 9-methylguanine–1-methylcytosine Watson-Crick base pair (designated as WC-[9MG·1MC + H]$^+$), from which dissociation pathways and dissociation energies were determined. Electronic structure calculations at the DFT, RI-MP2 and DLPNO-CCSD(T) levels of theory were used to identify product structures and delineate reaction mechanisms. Intra-base-pair proton transfer (PT) of WC-[9MG·1MC + H]$^+$ results in conventional base-pair conformations that consist of hydrogen-bonded [9MG + H]$^+$ and 1MC and proton-transferred conformations that are formed by PT from the N1 of [9MG + H]$^+$ to the N3′ of 1MC. Two types of conformers were distinguished by CID in which the conventional conformers produced [9MG + H]$^+$ product ions whereas the proton-transferred conformers produced [1MC + H]$^+$. The conventional conformers have a higher population (99.8%) and lower dissociation energy than the proton-transferred counterparts. However, in contrast to what was expected from statistical dissociation of the equilibrium base-pair conformational ensemble, the CID product ions of WC-[9MG·1MC + H]$^+$ were dominated by [1MC + H]$^+$ rather than [9MG + H]$^+$. This finding, alongside the non-statistical CID reported for deprotonated guanine–cytosine (Lu et al.; *PCCP*, 2016, **18**, 32222) and guanine–cytosine radical cation (Sun et al.; *PCCP*, 2020, **22**, 14875), reinforces that non-statistical dissociation is a distinctive feature of singly-charged Watson-Crick guanine–cytosine base pairs. It implies that intra-base-pair PT facilitates the formation of proton-transferred conformers in these systems and the ensuing conformers have loose transition states for dissociation. Monohydrate of WC-[9MG·1MC + H]$^+$ preserves non-statistical CID kinetics and introduces collision-induced methanol elimination via the reaction of the water ligand with a methyl group.

* E-mail: jianbo.liu@qc.cuny.edu. Tel: 1-718-997-3271.

1. Introduction

Since Löwdin[1] pointed out that proton transfer (PT) within the Watson-Crick (WC)[2] base pairs of DNA may be critically involved in genetic mechanism as a source of point spontaneous mutations, intra-base-pair PT has become a topic of substantial experimental work[3-16] and theoretical modeling.[14, 16-44] The underlying biological rationale is that the genetic information is encoded in the arrangement of intra-base-pair hydrogen-bond (H-bond) motif. Intra-base-pair PT leads to the formation of rare nucleobase tautomers (e.g. 6-hydroxyguanine (an enol tautomer of guanine)–4-iminocytosine (an imino tautomer of cytosine)) and consequently the change of the complementarity between nucleobases during replication (e.g., a universal mutation of 6-hydroxyguanine–4-iminocytosine to adenine (A)–thymine(T) that was found in bacteria, fungi, plants and animals[45]). Intra-base-pair PT also participates in radiation-induced DNA damage[14, 20] and in base-pair reactions with other molecules such as water and O_2.[6, 46] Besides its biological significance, intra-base-pair PT tailors charge transfer within DNA double helix[47] and in DNA-templated nanowires.[48]

In a neutral base pair, intra-base-pair PT in one direction induces another PT in the opposite direction[1, 21, 23, 34, 36, 42, 43] in order to balance the charge between the two base moieties. But anti-parallel double PT becomes unfeasible once one of the nucleobases obtains an additional charge. In the latter case, single PT becomes energetically favorable.[21] This was observed in protonated guanine–cytosine ($[G{\cdot}C + H]^+$),[10, 15, 17, 24, 32, 38, 41, 49, 50] deprotonated guanine–cytosine ($[G{\cdot}C - H]^-$),[12, 40] guanine–cytosine radical cations ($[G{\cdot}C]^{\bullet+}$),[3-6, 8, 11, 13, 14, 16, 18, 20-22, 25, 27, 29, 30, 37] guanine–cytosine radical anions ($[G{\cdot}C]^{\bullet-}$),[9, 22, 28, 31, 35, 39] hydride adducts of guanine–cytosine ($[G{\cdot}C + H]^-$),[26, 38] and metal cation-complexed guanine–cytosine.[44] As a result, a charged guanine–cytosine base pair is composed of a mixture of canonical conformation (hereafter referred to as conventional conformer) and proton-transferred conformation (formed by PT from the N1 site of guanine to the N3′ site of cytosine, referred to as PT conformer).

We have recently reported collision-induced dissociation (CID) of the WC-type deprotonated guanine–cytosine ($[G{\cdot}C - H]^-$) and deprotonated 9-methylguanine–cytosine ($[9MG{\cdot}C - H]^-$) base pairs in

the gas phase,[12] aimed to examine base-pair structures and intra-base-pair PT kinetics. More recently, we have carried out a similar CID measurement of the WC-type 9-methylguanine–1-methylcytosine base-pair radical cation ([9MG·1MC]$^{\bullet+}$) in the gas phase.[16] For each of these base-pair systems, the conventional and its corresponding PT conformers are close in energy (within 0.05 eV) and may interconvert via a low-energy barrier. Their respective structures were distinguished by the measurement of their CID product ions. In the case of [9MG·C – H]$^-$, the conventional structure 9MG·[C – $H_{N1'}$]$^-$ (i.e. deprotonated at the N1′ site of cytosine) dissociates into neutral 9MG and deprotonated [C – $H_{N1'}$]$^-$; whereas the PT structure [9MG – H_{N1}]$^-$·[1MC – $H_{N1'}$ + $H_{N3'}$] dissociates into deprotonated [9MG – H_{N1}]$^-$ and neutral 3H-keto-amino-cytosine. In the case of [9MG·1MC]$^{\bullet+}$, the conventional structure 9MG$^{\bullet+}$·1MC dissociates into 9MG$^{\bullet+}$ radical cation and neutral 1MC; whereas its PT structure [9MG – H_{N1}]$^{\bullet}$·[1MC + $H_{N3'}$]$^+$ dissociates into neutral [9MG – H_{N1}]$^{\bullet}$ radical and protonated [1MC + $H_{N3'}$]$^+$. For each system, the dissociation asymptote of the conventional structure is equal to or lower than that of the PT structure, and no reverse activation barrier was found in the dissociation of either structure. Surprisingly, the base-pair CID product ions were always overwhelmingly dominated by the fragments generated from a PT structures, i.e., [9MG – H_{N1}]$^-$ dominated the CID of [9MG·C – H]$^-$ while [1MC + $H_{N3'}$]$^+$ dominated the CID of [9MG·1MC]$^{\bullet+}$ as verified by both experimental measurements[12,16] and molecular dynamics simulations.[40] Such experimental and theoretical results are contrary to statistical dissociation kinetics.

Inspired by these intriguing discoveries, we have extended investigation to protonated guanine–cytosine base pair and its monohydrate in the present work. The motivation was to determine whether non-statistical CID is the nature of guanine–cytosine base pairs regardless of their charge and electron spin states. One unique feature of protonated guanine–cytosine is that it may adopt WC and/or Hoogsteen[51]-type base pairing,[15, 49, 52, 53] as illustrated for protonated 9-methylguanine–1-methylcytosine ([9MG·1MC + H]$^+$) in Scheme 1. CID and infrared multiphoton dissociation of Hoogsteen-type [9MG·1MC + H]$^+$ and [9-ethylguanine·1MC + H]$^+$ in the gas phase were recently reported by other

groups.[15, 54, 55] The present work focuses on the experimental and theoretical study of WC-[9MG·1MC + H]$^+$ and the comparison of this species with its deprotonated and radical cation analogues.

Guided-ion beam tandem mass spectrometry was used to conduct CID of WC-[9MG·1MC + H]$^+$ and its monohydrate WC-[9MG·1MC + H]$^+$·H_2O. Xe was chosen as the collision gas to eliminate complications from the chemistry of target gas. Experimental measurements included CID product ion distributions and cross sections at different center-of-mass collision energies (E_{col}), from which dissociation pathways and dissociation threshold energies of WC-[9MG·1MC + H]$^+$·$(H_2O)_{0,1}$ were determined. To interpret experimental data and provide insight into intra-base-pair reactions, ab initio and density functional theory (DFT) computations were utilized to construct reaction coordinates and potential energy diagrams.

2. Experimental and Theoretical Section

2.1 Instrumentation and measurement

2.1.1 CID product ions and cross sections. Formation and CID of gas-phase base-pair ions were carried out on a home-built guided-ion beam tandem mass spectrometer. The apparatus consists of an electrospray ionization (ESI) ion source, a radio-frequency (rf) hexapole ion guide, a quadrupole mass filter, a rf octopole ion guide surrounded by a scattering cell, a second quadrupole mass filter and a pulse-counting electron-multiplier ion detector. Details of the instrument can be found in previous reports.[12, 56]

Similar to our previous work,[12, 16] 9MG and 1MC were used as prototype substrates of deoxyguanosine and deoxycytidine as the methyl group mimics the sugar group in nucleosides. Gas-phase [9MG·1MC + H]$^+$ ions were generated by ESI. As verified by differential ion mobility spectra and infrared multiphoton dissociation spectra,[15, 54] WC-[9MG·1MC + H]$^+$ was preferentially produced (91%) from an ESI solution of pH 5.8 whereas Hoogsteen-[9MG·1MC + H]$^+$ predominated (66%) from a solution of pH 3.2 (when 1MC is protonated prior to pairing with 9MG[53]). Accordingly, in the present work WC-type [9MG·1MC + H]$^+$ was prepared by mixing 0.5 mM 9MG (Chemodex, > 98%) and 0.5 mM 1MC (Enamine, 95%) in HPLC grade methanol/water (v : v = 3:1).

The base-pair solution was pumped through an electrospray needle at a flow rate of 0.04 mL/h. The electrospray needle was maintained at 2.5 kV with respect to the ground. The resulting positively charged spray of fine droplets entered the source chamber of the mass spectrometer through a pressure-reducing desolvation capillary which is located 7 mm away from the emission tip of the ESI needle. The capillary was biased at 126 V. Liquid converted to gas-phase ions after passing through the heated capillary and were transported into the source chamber that was evacuated to a pressure of 1.8 Torr. A skimmer with an orifice of 1.5 mm is located at 3 mm away from the capillary end, separating the source chamber and the hexapole ion guide. The skimmer was biased at 24 V relative to the ground. The electrical field between the capillary and the skimmer introduced collision-induced desolvation of solvated ions and hence removed residual solvent molecules. Under mild heating and collision conditions, not all of the solvent was evaporated, resulting in hydrated base-pair ions. In this experiment, the capillary was heated to 138 °C for producing the maximum intensity of WC-$[9MG{\cdot}1MC + H]^+$ and to 134 °C for WC-$[9MG{\cdot}1MC + H]^+{\cdot}H_2O$.

Ions emerging from the skimmer were transported into the hexapole at a pressure of 24 mτ. Interaction of ions with the background gas within the hexapole led to collisional focusing and thermalization of ions to ~ 310 K. Ions subsequently passed into a mass-selecting quadrupole for selection of reactant ions. The mass-selected base-pair ions were collected and collimated by a set of electrostatic lenses. The combination of collisional damping within the hexapole and the controlled collection radius at the quadrupole exit produced a mass-selected ion beam with a narrow kinetic energy spread (0.7 eV or less). Ion beam intensities were 3×10^4 count per sec for WC-$[9MG{\cdot}1MC + H]^+$ and 3×10^3 count per sec for WC-$[9MG{\cdot}1MC + H]^+{\cdot}H_2O$.

Mass-selected base-pair ions were injected into the octopole ion guide which trapped ions in the radial direction. The octopole was surrounded by a 10-cm scattering cell which was filled with Xe (Spectral Gases, 99.995%). The cell pressure was set at 0.01 mτ using a leak valve and continuously measured using a MKS Baratron capacitance manometer. Under our experimental conditions, base-pair ions

underwent at most a single collision with Xe within the scattering cell.

In addition to rf voltages, DC bias voltage of variable amplitude was applied to the octopole ion guide. DC voltage was used to control the kinetic energy of the ions in the laboratory frame (E_{lab}), thereby setting the collision energy (E_{col}) between the ions and the collision gas in the center-of-mass frame, that is $E_{col} = E_{lab} \times m_{neutral}/(m_{ion} + m_{neutral})$ where $m_{neutral}$ and m_{ion} are the masses of neutral collision gas and ions, respectively. CID of base-pair ions was conducted at various E_{col}. Fragment ions and the remaining base-pair ions drifted to the end of the octopole, and were mass analyzed by the second quadrupole and counted by the electron multiplier. Product ion cross sections were calculated from the ratios of reactant and product ion intensities, the collision gas pressure in the scattering cell and the effective length of the scattering cell. The entire experiment was repeated four times to reduce measurement uncertainty.

2.1.2 Dissociation threshold energies. Due to the kinetic energy spread and the internal energy of the primary ion beam, cross sections of CID product ions rise from zero at E_{col} before true dissociation thresholds (E_0). To extract an accurate value of E_0, a modified line-of-centers (LOC) model[57-60] was assumed for the E_{col} dependence of "true" cross section $\sigma(E_{col}) = \sigma_0 \frac{(E_{col} + E_{vib} + E_{rot} - E_0)^n}{E_{col}}$, where σ_0 is an energy-independent scaling factor, E_{vib} and E_{rot} are reactant vibrational and rotational energies, E_0 is as defined above, and n is a fitting parameter used to adjust the slope of $\sigma(E_{col})$. This model assumes that, at the energies near E_0, at least some of the collisions are completely inelastic so that E_{col} is all converted to internal energy to drive CID. This was verified in the threshold CID of $[9MG{\cdot}C - H]^-$, $[9MG{\cdot}1MC]^{\bullet+}$ and many other ions. [12, 16, 59]

$\sigma(E_{col})$ needs to integrate over experimental broadening and various kinetic factors. A Monte Carlo ion-molecule collision simulation program,[61] described in our recent work,[16] was used to mimic the experimental conditions: Xe atoms were sampling a Maxwell-Boltzmann velocity distribution at 300 K; the WC-$[9MG{\cdot}1MC + H]^+$ ion beam had a kinetic energy spread of 0.7 eV, and the ion E_{vib} and E_{rot} were sampled at a temperature of 310 K. For each product channel, collisions of base-pair ion with Xe were simulated as a function of E_{col} (100000 collisions under each condition). The established distributions of

target gas velocities, and the ion kinetic energy, E_{vib} and E_{rot} were then sampled into cross section fitting. Due to the large size of WC-[9MG·1MC + H]$^+$, a kinetic shift was expected in the near-threshold collisions — that is energy in excess of E_0 was required to produce dissociation within the experimental time scale (~500 μs).[62] To this end, a Rice–Ramsperger–Kassel–Marcus (RRKM, see below)[63] model was included in the fitting to decide whether each collision led to detectable dissociation. A leveling-off collision energy was used in the fitting so that $\sigma(E_{col})$ would reach a plateau at high E_{col}. The rising curvature of $\sigma(E_{col})$ depends sensitively on E_0 and n, and their values were adjusted until the convoluted $\sigma(E_{col})$ reached the best agreement with experimental data.

2.2 Computational Modeling

2.2.1 Reaction coordinates and potential energy diagrams. WC-[9MG·1MC + H]$^+$ presents multiple conformations due to keto-enol isomerization, intra-base-pair PT, and protonation at different sites. Prior to reaction coordinate computation, it was warranted to identify all possible conformations of WC-[9MG·1MC + H]$^+$ and use the appropriate ones as the starting geometries in theoretical modeling. Our conformation search was carried out at the ωB97XD/6-311++G(d,p) level of theory using Gaussian 09.[64] The ωB97XD[65] functional is able to mitigate self-interaction errors and improves the orbital descriptions of ionic species.[37] The basis set superposition errors (BSSEs)[66] for the base-pair structures are less than 0.05 eV at ωB97XD/6-311++G(d,p); for comparison, BSSEs are 0.08 eV at B3LYP/DZP^{++}.[67] Thereby the BSSEs have no influence on the order of stability of various conformers.

Reaction coordinate was initiated at the lowest-energy base-pair conformer, both in the absence and the presence of a water ligand. Structures of reactants, intermediate complexes, transition states (TSs) and dissociation products were fully optimized at the ωB97XD/6-311++G(d,p) level of theory. All TSs were verified as first-order saddle points, and the only imaginary frequencies in TSs are associated with vibration along the anticipated reaction coordinate. Intrinsic reaction coordinate calculations were carried out to ascertain that TSs are connected to correct reactant/product minima.

To validate reaction potential energies calculated at ωB97XD/6-311++G(d,p), electronic energies of

the ωB97XD/6-311++G(d,p)-optimized structures were recalculated using a larger basis set aug-cc-pVQZ and with the B3LYP functional. To prevent any biases that could possibly raise from the DFT calculations, reaction energies were further evaluated using the following two additional theories. The resolution-of-the-identity second-order Møller-Plesset perturbation theory (RI-MP2) with the aug-cc-pVTZ basis set which is to provide accurate description of H-bonds,[68, 69] and the domain based local pair-natural orbital coupled-cluster single-, double- and perturbative triple-excitations method (DLPNO-CCSD(T)) with the aug-cc-pVTZ basis set which serves as a reference for the accuracy of base-pair interaction energies.[70] Electronic energies at these levels of theory were accomplished using ORCA 4.0.1.[71] Reaction enthalpies reported at each level is the summation of the electronic energies calculated at the specified level and the 298 K thermal corrections calculated at ωB97XD/6-311++G(d,p) (including zero-point energies which was scaled by a factor 0.975[72]).

2.2.2 Statistical kinetics modeling. RRKM theory was used to predict statistical reaction outcomes. This theory was based on the assumption that energy is randomized and distributed statistically among all of the energetically accessible states in the system, and the rate of a particular dissociation process is proportional to the total number of energetically accessible states at the TS.[73, 74] A statistical reaction occurs via the minimum-energy pathway on the reaction potential energy surface (PES)[75] with a rate constant $k_{diss}(E,J) = \frac{d\sum_{K=-J}^{J} G[E - E_0 - E_r^{\dagger}(J,K)]}{h \sum_{K=-J}^{J} N[E - E_r(J,K)]}$, where d is the reaction path degeneracy, G is the sum of accessible states from 0 to $E - E_0 - E_r^{\dagger}$ at the TS, N is the density of states in the energized reactant, E is the system energy, E_0 is the unimolecular dissociation threshold, E_r and $E_r^{\dagger}$ are the rotational energies of the reactant and the TS, J is the angular momentum quantum number, and K is the rotation quantum number.[76] Calculation of k_{diss} was carried out using the Zhu and Hase version of the RRKM program,[77] in which density of states was calculated by direct count algorithm. All $(2J + 1)$ K-levels were treated active and counted in $k_{diss}(E, J)$.

3. Results and Discussion

3.1 Structures of WC-[9MG·1MC + H]$^+$·$(H_2O)_{0,1}$

We have identified 25 conformers for WC-[9MG·1MC + H]$^+$ within an energy range of 4.4 eV at the ωB97XD/6-311++G(d,p) level of theory. Structures and relative formation enthalpies (ΔH at 298 K, with respect to the global minimum) of these conformers are summarized in Figure 1. Their Cartesian coordinates are provided in the Supporting Information. The most preferred protonation site at WC-9MG·1MC is the N7 site of 9MG, followed by O6 and N3, then N2 and finally C8, C5 and C4 of 9MG. It is also possible to protonate the 1MC moiety at its O2′, C5′ or C6′ site. The global minimum WC-[9MG·1MC + H]$^+$_1 is protonated at the N7 of 9MG and adopts a conventional structure in which the central H is covalently bound to the N1 of 9MG. Of the 25 WC-type conformers, WC-[9MG·1MC + H]$^+$_1 accounts for an overwhelming majority in thermal equilibrium with a population > 99.8%. Considering that Hoogsteen-type structure accounted for less than 9% of the ESI-generated [9MG·1MC + H]$^+$ ion beam under our experimental condition.[15] It is reasonable to use WC-[9MG·1MC + H]$^+$_1 as the representative reactant ion structure. This conformer is referred to as WC-[9MG + H_{N7}]$^+$·1MC in the remainder of the paper. The second lowest-energy conformer WC-[9MG·1MC + H]$^+$_2, lying in energy 0.17 eV above the global minimum, has the central H transferred from the N1 of 9MG to the N3′ of 1MC and is referred to as WC-[9MG + H_{N7} – H_{N1}]·[1MC + $H_{N3'}$]$^+$ hereafter. WC-[9MG + H_{N7} – H_{N1}]·[1MC + $H_{N3'}$]$^+$ did not present in the ESI-generated reactant ion beam, but it could form in the collisional activation of WC-[9MG + H_{N7}]$^+$·1MC. Protonation at the O6 of 9MG with the proton pointing towards 1MC (i.e. *trans*-) causes the sliding of the two bases against each other and results in new central H-bonds (O6···H···N3′ and N1···H···O2′) in WC-[9MG·1MC + H]$^+$_3 and 4. A number of conformers can interconvert between each other by inter-base-pair PT, as indicated in Figure 1. Our conformation search not only reproduced the conformations reported at the other levels of theory[17, 24, 32, 38, 41, 67, 78] but identified many new ones.

Initial geometries for the monohydrated base pairs were obtained by adding a water molecule to all of the possible hydration sites at WC-[9MG + H_{N7}]$^+$·1MC. The starting geometries were then optimized at the ωB97XD/6-311++G(d,p) level of theory. The converged monohydrate structures are reported in

Figure 2, together with their ΔH (relative to the global minimum) and hydration enthalpies ($\Delta H_{hydration} = \Delta H_{hydrate} - \Delta H_{dry\ ion} - \Delta H_{water}$) at 298 K. Their Cartesian coordinates are provided in the Supporting Information. The hydration sites identified at WC-[9MG + H_{N7}]$^+$·1MC resemble those in the deprotonated,[12] neutral,[35, 79, 80] radical cation,[16] or radical anion[35] forms of WC-9MG·1MC. In some monohydrates, hydration energy arises from charge-dipole interaction, such as WC-[9MG + H_{N7}]$^+$·1MC_2 and 5.

The lowest-energy monohydrate, WC-[9MG·1MC + H]$^+$·H_2O_1, has a water ligand bound to the O6 and N7-H of [9MG + H_{N7}]$^+$ with $\Delta H_{hydration}$ of -0.69 eV. This structure represents a predominant population (> 90%) of the monohydrated reactant ions and is referred to as WC-[9MG + H_{N7}]·1MC·H_2O hereafter. We found that, in the case of [9MG·1MC]$^{\bullet+}$, monohydration could reverse the populations of the conventional vs. the PT structures. This, however, does not occur in WC-[9MG·1MC + H]$^+$. The monohydrated PT conformers lie in energy ~ 0.16 eV above their conventional counterparts, therefore their presence in the primary ion beam could be ignored.

3.2 CID of WC-[9MG + H_{N7}]$^+$·1MC

3.2.1 Products, cross sections and dissociation thresholds. The CID product ions of WC-[9MG + H_{N7}]$^+$·1MC + Xe include protonated [9MG + H]$^+$ at *m/z* = 166 and protonated [1MC + H]$^+$ at *m/z* = 126, as shown by a CID product ion mass spectrum measured at 3.0 eV in Figure 3a. The fact that [1MC + H]$^+$ was detected in the products implies the formation of PT isomer(s) from WC-[9MG + H_{N7}]$^+$·1MC in the collisional activation. Figures 3b and c shows the individual cross sections for the two product ions over an E_{col} range from 0.05 – 6.0 eV. Error bars for the cross sections were determined on the basis of the four sets of measurement. The solid lines in Figures 3b and c are the LOC-model-based $\sigma(E_{col})$ fits to the experimental data, taking into account the internal energy distributions and the kinetic energy spreads of the reactant ion beam and the collision gas. The values of the best fit E_0 are indicated in the figures. E_0 for [9MG + H_{N7}]$^+$·1MC → [9MG + H_{N7}]$^+$ + 1MC (Figure 3b) was determined to be 1.7 eV with the fitting parameter *n* equal to 2.0 and the leveling-off energy at 2.6 eV.

The cross section for $[1MC + H]^+$ (Figure 3c) appears to consist of two components, with one dominating at the low energy range and the other starting to become dominant at higher energies. No satisfactory fit was obtained to the cross section using only a single $\sigma(E_{col})$ function. We therefore fit the cross section using two sets of $\sigma(E_{col})$ functions. E_0 and n of each set were adjusted independently to obtain the best fit to the total cross section. As shown by the green and blue curves in Figure 3c, the first component has E_0 = 1.8 eV, n = 2.0 and leveling off energy at 2.5 eV, and the second component has E_0 = 2.6 eV, n = 2.1 and leveling off energy at 4.6 eV. The sum of the two fits is presented by the black curve. According to the fitting results, the cross section of the low-energy channel reaches a plateau at 2.5 eV. The high-energy channel becomes dominant starting at 3.6 eV, with its cross section being a factor of 2 higher than the low-energy channel at 6.0 eV.

The abundance of $[1MC + H]^+$ in the product ions is much higher than that of $[9MG + H]^+$ at all collision energies. To examine the correlation between the two product ion channels, the branching ratio of $[1MC + H]^+/[9MG + H]^+$ was calculated as a function of E_{col} and plotted in Figure 4a. The ratio is around 1.2 at E_{col} = 2.0 eV and raises up to 3.4 at 6.0 eV, indicating that more $[1MC + H]^+$ was produced with the increasing of E_{col}. In other words, intra-base-pair PT prevails within protonated guanine–cytosine. A similar scenario was observed in the CID of $[9MG{\cdot}1MC]^{\bullet+}$radical cation[16] and $[9MG{\cdot}C - H]^-$ anion.[12] For the purpose of comparison, the product ion branching ratios for the latter two base-pair systems are presented in Figure 4b and c. For all reaction systems, branching ratios were calculated as the product ions produced from a PT base-pair structure vs. the product ions produced from a conventional base-pair structure. This corresponds to $[1MC + H]^+/9MG^{\bullet+}$ for $[9MG{\cdot}1MC]^{\bullet+}$ in Figure 4b, and $[9MG - H]^-/[C - H]^-$ for $[9MG{\cdot}C - H]^-$ in Figure 4c.

3.2.2 Reaction coordinate. Figure 5 summarizes the base-pair reactions originating at WC-$[9MG + H_{N7}]^+{\cdot}1MC$, where the starting reactant is located at zero energy. Reaction potential energetics were calculated at the ωB97XD/6-311++G(d,p), ωB97XD/aug-cc-pVQZ, B3LYP/aug-cc-pVQZ, RI-MP2/aug-cc-pVTZ and DLPNO-CCSD(T)/aug-cc-pVTZ levels of theory. The results obtained using the five

methods are compiled in Table 1. A good agreement was achieved among the different levels of theory, except for the B3LYP method that systematically underestimated dissociation energies. The DLPNO-CCSD(T) results represent the highest level of theory we used and have matched the experimental dissociation threshold energies. These values were thus adopted in reaction PES and kinetics analysis.

The energetically most favorable intra-base-pair reaction corresponds to the formation of WC-[9MG + H_{N7} – H_{N1}]·[1MC + $H_{N3'}$]$^+$ via WC-TS_PT1, as shown in Figure 5a. Each of WC-[9MG + H_{N7}]$^+$·1MC and WC-[9MG + H_{N7} – H_{N1}]·[1MC + $H_{N3'}$]$^+$ may eliminate the neutral base, leading to the formation of [9MG + H_{N7}]$^+$ and [1MC + H_{N3}]$^+$ fragment ions, respectively. Shown in Figure 5b are the intra-base-pair reactions initiated by keto-enol isomerization of WC-[9MG + H_{N7}]$^+$·1MC to WC-[9MG + H_{O6}]$^+$·1MC via WC-TS-enol. WC-[9MG + H_{O6}]$^+$·1MC undergoes intra-base-pair PT via WC-TS_PT1_enol and produces WC-[9MG + H_{O6} – H_{N1}]·[1MC + $H_{N3'}$]$^+$. WC-[9MG + H_{O6}]$^+$·1MC and WC-[9MG + H_{O6} – H_{N1}]·[1MC + H_{N3}]$^+$ are higher in energy than WC-[9MG + H_{N7}]$^+$·1MC by 0.28 and 0.33 eV, respectively. CID products and threshold energies mediated by the four base-pair conformers are summarized below:

WC-[9MG + H_{N7}]$^+$·1MC

$\rightarrow$ [9MG + H_{N7}]$^+$ + 1MC $\Delta H = 1.65$ eV (1a)

$\rightarrow$ WC-[9MG + H_{O6}]$^+$·1MC $\rightarrow$ [9MG + H_{O6}]$^+$ + 1MC $\Delta H = 1.90$ eV (1b)

$\rightarrow$ WC-[9MG + H_{N7} – H_{N1}]·[1MC + $H_{N3'}$]$^+$ $\rightarrow$ [9MG + H_{N7} – H_{N1}] + [1MC + $H_{N3'}$]$^+$ $\Delta H = 2.50$ eV (2a)

$\rightarrow$ WC-[9MG + H_{O6} – H_{N1}]·[1MC + $H_{N3'}$]$^+$ $\rightarrow$ [9MG + H_{O6} – H_{N1}] + [1MC + $H_{N3'}$]$^+$ $\Delta H = 1.70$ eV (2b)

Because the difference between the dissociation energies of reaction 1a and b is small, we were not able to distinguish these two reaction pathways in the cross section of [9MG + H]$^+$. On the other hand, we have indeed revealed two reaction pathways in the cross section of [1MC + H]$^+$ (see Figure 3c). The LOC model-fitted dissociation thresholds (2.6 eV and 1.8 eV) have closely matched the calculated energetics of reaction 2a and 2b. The combination of cross-section measurement and reaction PES has revealed the following fact: (1) despite that the WC-[9MG + H_{N7}]$^+$·1MC conformer has the exclusive abundance in the reactant ion beam and has the lowest dissociation energy, the products of [9MG + H_{N7}]$^+$

+ 1MC account for only one-third of the total base-pair dissociation; (2) the dominant dissociation mechanism leads to the formation of 9MG + [1MC + H]$^+$. This product channel is mediated by reaction 2b at low E_{col}, switching over to reaction 2a at high E_{col}.

3.2.3 Kinetics of WC-[9MG·1MC + H]$^+$ and comparison with [9MG·1MC]$^{\bullet+}$ and [9MG·C – H]$^-$. We have recently reported[12, 16] a non-statistical regime in the CID of [9MG·1MC]$^{\bullet+}$ and [9MG·C – H]$^-$, wherein the dissociation originating at their PT conformers dominated the products as shown in Figure 4b and c. In the present work, the CID of WC-[9MG·1MC + H]$^+$ was also dominated by its PT conformers. This raises two closely related questions: why does CID of guanine–cytosine prefer to occur at a PT conformer regardless of base-pair ionization state and relative stability? And does that reflect a competition of thermodynamic vs. kinetic reaction control in conventional and PT conformers? Both questions hinge on two factors: the probability of forming different base-pair conformers and the dissociation rate of each conformer.

To determine if non-statistical CID occurred in WC-[9MG·1MC + H]$^+$ or not, thermodynamical product branching ratio of [1MC + H]$^+$/[9MG + H]$^+$ was calculated by $\sum_i (DOS_{PT\ complex\ i} \times k_{PT\ complex\ i}) / \sum_i (DOS_{Conventional\ complex\ i} \times k_{Conventional\ c\ omplex\ i})$. DOS is the density of states for individual conventional and PT base-pair conformers that have participated in the reaction. The value of DOS reflects the relative formation efficiency of each conformer in collisional activation, and it determines the contribution of each complex if interconversion is facile. k is the RRKM dissociation rate constant for each conformer. All of the four conformers WC-[9MG + H_{N7}]$^+$·1MC, WC-[9MG + H_{O6}]$^+$·1MC, WC-[9MG + H_{N7} – H_{N1}]·[1MC + $H_{N3'}$]$^+$ and WC- [9MG + H_{O6} – H_{N1}]·[1MC + $H_{N3'}$]$^+$ are included in the modeling. As DOS and k are E_{col} dependent, their values were calculated as a function of E_{col} from 2.0 eV to 6.0 eV. Since there are no reverse barriers for base-pair dissociation, vibrational frequencies appropriate to the dissociation TSs were estimated for two hypothetical reaction scenarios.[62, 81-84] In one reaction scenario, vibrational frequencies of the so-called ″tight″ TS were adopted from those of the starting base-pair conformer with the removal of the symmetric stretching frequency of the WC H-bonds

as it represents the reaction coordinate for base-pair dissociation. In the other reaction scenario, a ″loose″ TS was assumed by keeping in the TS all of the frequencies that are partitioned into dissociation products (referred to as conserved modes[85] as they exhibit little changes in the dissociation). Of the remaining six translational modes[85] which are lost upon dissociation, the symmetric stretching of the WC H-bonds was removed. The other five modes (i.e., out-of-plane twisting, out-of-plane butterfly bending, anti-symmetric out-of-plane bending/step, in-plane bending/gearing and anti-symmetric stretching of the two bases with respect to each other) become intermolecular motions and their frequencies were scaled by 0.5 to account for the looseness of TS and the dissociation entropies. The choice of this scaling factor was based on representative work on the statistical treatment of weakly bonded complexes.[16, 81-83]

Two sets of RRKM results, which were obtained from the tight and loose TS-based RRKM modeling, respectively, are presented in Figure 4a. The two sets have predicted nearly identical dissociation product branching for WC-[9MG·1MC + H]$^+$. According to these two models, the branching ratio of [1MC + H]$^+$/[9MG + H]$^+$ increases with E_{col}, but the predicted values are an order of magnitude lower than the experimental measurement. The most significant problem is that [9MG + H]$^+$ dominates the product ions in a statistical mechanism whereas [1MC + H]$^+$ represents the major product ions in the experiment. In addition, RRKM has predicted that the formation of [1MC + H]$^+$ occurs only via reaction 2b, while in the experiment reaction 2a has suppressed reaction 2b at high E_{col} as evidenced by the presence of two pathways in the cross section of [1MC + H]$^+$ (see Figure 3c).

In the direct dynamics trajectory simulation of the CID of deprotonated guanine–cytosine,[40] we found that the proton-transferred base-pair conformer dissociated faster (via a less tight TS) than the conventional conformer. To test this idea in the CID of WC-[9MG·1MC + H]$^+$, we did a third set of RRKM calculations where the tightness of individual dissociation TSs were adjusted to bring the calculated product branching ratios into agreement with the experiment. To this end, relatively ″tight″ dissociation TSs were assumed for the two conventional conformers (i.e., WC-[9MG + H_{N7}]$^+$·1MC and WC-[9MG + H_{O6}]$^+$·1MC) by increasing the frequency scaling factor to 0.75 for the aforementioned five

translational modes. Meanwhile, a more ″loose″ TS was assumed for WC-[9MG + H_{N7} – H_{N1}]·[1MC + $H_{N3'}$]$^+$ by decreasing the frequency scaling factor to 0.25 and increasing the central H-bond lengths by 5%. The idea was to find and factor into reactions some kinetic control. The result of this empirically adjusted RRKM calculation is indicated as mixed-TS RRKM in Figure 4a.

The adjusted RRKM calculation indeed results in the right magnitude and E_{col} dependence of the product branching ratios, except that the RRKM prediction deviates from the experiment at the lowest E_{col}. The latter deviation is not unexpected because the experimental E_{col} distribution is 0.2 eV wide. Comparison of the three RRKM modeling results with the experiment emphasizes an important point that the properties of the dissociation TSs differ in different conformers. Specifically, the PT conformer may adopt a looser dissociation TS than the conventional conformer in order to produce the measured product distribution.

Finally, while all of WC-[9MG·1MC + H]$^+$, [9MG·1MC]$^{\bullet+}$ and [9MG·C – H]$^-$ have presented anomalous CID product distributions and favored the dissociation of their PT conformers, WC-[9MG·1MC + H]$^+$ has presented difference E_{col} dependence of the product branching ratio than the two analogues, i.e., the dominance of [1MC + H]$^+$ becomes more remarkable at high E_{col}. This is due to the fact that each of [9MG·1MC]$^{\bullet+}$ and [9MG·C – H]$^-$ involves only one conventional and one PT conformers in collisional activation, i.e., 9MG$^{\bullet+}$·1MC ⇌ [9MG – H_{N1}]$^{\bullet}$·[1MC + $H_{N3'}$]$^+$ and 9MG·[1HC – $H_{N1'}$]$^-$ ⇌ [9MG – H_{N1}]$^-$·[1HC – $H_{N1'}$ + $H_{N3'}$]. On the other hand, WC-[9MG·1MC + H]$^+$ forms two conventional and two PT conformers (due to keto-enol isomerization) in collisional activation and has more dissociation pathways available, of which reaction 2a of high-E_0 opens at high collision energies as another result of non-statistical kinetics.

3.3 Reactions of WC-[9MG + H_{N7}]$^+$·1MC·H_2O

The fragment ions of WC-[9MG + H_{N7}]$^+$·1MC·H_2O + Xe were detected at m/z 291, 277, 166 and 126, as demonstrated in Figure 6. Assignments of these product ions, their possible formation pathways and the associated reaction ΔHs (calculated at DLPNO-CCSD(T)/aug-cc-pVTZ//ωB97XD/6-311++G(d,p))

are listed below.

$WC\text{-}[9MG + H_{N7}]^+ \cdot 1MC \cdot H_2O$

$\rightarrow WC\text{-}[9MG + H_{N7}]^+ \cdot 1MC$ (*m/z* 291) + H_2O $\Delta H = 0.62$ eV (3a)

$\rightarrow WC\text{-}[9MG + H_{N7} - H_{N1}] \cdot [1MC + H_{N3'}]^+$ (*m/z* 291) + H_2O $\Delta H = 0.78$ eV (3b)

$\rightarrow WC\text{-}[9MG + H_{O6}]^+ \cdot 1MC$ (*m/z* 291) + H_2O $\Delta H = 0.90$ eV (3c)

$\rightarrow WC\text{-}[9MG + H_{O6} - H_{N1}] \cdot [1MC + H_{N3'}]^+$ (*m/z* 291) + H_2O $\Delta H = 0.95$ eV (3d)

$\rightarrow [9MG + H_{N7}]^+$ (*m/z* 166) + 1MC + H_2O $\Delta H = 2.27$ eV (4a)

$\rightarrow [9MG + H_{O6}]^+$ (*m/z* 166) + 1MC + H_2O $\Delta H = 2.52$ eV (4b)

$\rightarrow [9MG + H_{N7} - H_{N1}] + [1MC + H_{N3'}]^+$ (*m/z* 126) + H_2O $\Delta H = 3.12$ eV (5a)

$\rightarrow [9MG + H_{O6} - H_{N1}] + [1MC + H_{N3'}]^+$ (*m/z* 126) + H_2O $\Delta H = 2.33$ eV (5b)

$\rightarrow WC\text{-}[9MG + H_{N7}]^+ \cdot 1HC$ (*m/z* 277) + CH_3OH $\Delta H = 1.16$ eV (6a)

$\rightarrow WC\text{-}[9MG + H_{N7} - H_{N1}] \cdot [1HC + H_{N3'}]^+$ (*m/z* 277) + CH_3OH $\Delta H = 1.34$ eV (6b)

$\rightarrow WC\text{-}[9HG + H_{N7}]^+ \cdot 1MC$ (*m/z* 277) + CH_3OH $\Delta H = 1.30$ eV (6c)

$\rightarrow WC\text{-}[9HG + H_{N7} - H_{N1}] \cdot [1MC + H_{N3'}]^+$ (*m/z* 277) + CH_3OH $\Delta H = 1.44$ eV (6d)

The CID product ion mass spectra were not able to distinguish different product ion structures of the same m/z, therefore the product cross sections of the same *m/z* were lumped together in Figure 7. Due to the extremely lower ion beam intensity of $WC\text{-}[9MG + H_{N7}]^+ \cdot 1MC \cdot H_2O$ at high collision energies, the cross sections were measured up to only 3.0 eV. Of the four product ions, water elimination (reactions 3a-d) is the energetically most favorable and dominates the dissociation of $WC\text{-}[9MG + H_{N7}]^+ \cdot 1MC \cdot H_2O$. Similar to what was observed in the CID of $WC\text{-}[9MG + H_{N7}]^+ \cdot 1MC$, product ions of $[1MC + H]^+$ (via reactions 5a-b) has larger cross sections than $[9MG + H]^+$ (via reaction 4a-b) in the CID of $WC\text{-}[9MG + H_{N7}]^+ \cdot 1MC \cdot H_2O$. Product ions of m/z 277 are due to the elimination of a methanol molecule from the monohydrated base pair via reactions 6a-d. This product represents a minor channel at all E_{col}. Each of the four product ions may involve multiple reaction pathways with different reaction threshold energies. For this reason, we did not attempt to extract individual reaction thresholds from the cross sections. But all product ions have the appearance energies which qualitatively comply with endothermic reactions.

The reaction pathways for intra-base-pair PT, keto-enol isomerization, water elimination, methanol elimination and base-pair dissociations of $WC\text{-}[9MG + H_{N7}]^+ \cdot 1MC \cdot H_2O$ are outlined in Figure 8. Their

reaction enthalpies (with respect to WC-[9MG + H_{N7}]$^{+}$·1MC·H_2O) were calculated at different levels of theory. The results are compiled in Table 2. Except for the aforementioned underestimated B3LYP energies, the deviation is 0.15 eV on average for the reaction ΔHs calculated at the other four levels of theory.

Figures 8a and b show a similar set of reaction pathways as Figure 5, except for the water elimination in the monohydrated base pairs. It is interesting to mention that the water ligand acts as a relay for proton transfer needed in the keto-enol isomerization of WC-[9MG + H_{N7}]$^{+}$·1MC → WC-[9MG + H_{O6}]$^{+}$·1MC, and consequently lowers the barrier of WC-TS_enol dramatically from 1.64 eV in the dry base pair to 0.28 eV in the monohydrated base pair. Similar to the dry base pair, kinetic reaction control competes with thermodynamic reaction control in the base-pair dissociation of WC-[9MG·1MC + H]$^{+}$·H_2O. Despite that the [9MG + H]$^{+}$ product ion is favored under thermodynamical control (i.e., it has lower E_0 than [1MC + H]$^{+}$), the product branching ratio of [1MC + H]$^{+}$/[9MG + H]$^{+}$ is clearly controlled by kinetics.

Figures 8c and d present collision-induced reactions between the water ligand and a methyl group in the base pair. In Figure 8c, the water reacts with the methyl group of 1MC by crossing the barrier of WC-TS1, forming WC-[9MG + H_{N7}]$^{+}$·1HC and a neutral methanol. The reaction appears to be initiated by a second-order nucleophilic substitution (S_N2) reaction wherein the departure of the N1′-methyl group occurs simultaneously with the attack of the water oxygen atom,[86, 87] followed by the transfer of a hydrogen atom from the water to the N1′ site. An alternative but similar S_N2 reaction mechanism is illustrated in Figure 8d wherein the water reacts with the methyl group of 9MG via WC-TS2 to form WC-[9HG + H_{N7}]$^{+}$·1MC and methanol. It is possible to distinguish the two reaction pathways of Figures 8c and d by using protonated 9-ethylguanine–1-methylcytosine base pair as the reactant ion. However, considering the similar energetic profiles and activation barriers of the two reaction pathways, it would be reasonable to expect both pathways in the experiment. Both WC-[9MG + H_{N7}]$^{+}$·1HC and WC-[9HG + H_{N7}]$^{+}$·1MC may undergo inter-base-pair PT to form WC-[9MG + H_{N7} – H_{N1}]·[1HC + $H_{N3'}$]$^{+}$ and WC-

$[9HG + H_{N7} - H_{N1}]\cdot[1MC + H_{N3'}]^+$, respectively. It is also possible that methanol elimination occurs via WC-$[9MG + H_{N7} - H_{N1}]\cdot[1MC + H_{N3'}]^+\cdot H_2O \rightarrow [9MG + H_{N7} - H_{N1}]\cdot[1HC + H_{N3}]^+ + CH_3OH$ with a TS of 3.89 eV or WC-$[9MG + H_{N7} - H_{N1}]\cdot[1MC + H_{N3'}]^+\cdot H_2O \rightarrow [9HG + H_{N7} - H_{N1}]\cdot[1MC + H_{N3}]^+ + CH_3OH$ with a TS of 3.70 eV. The cross sections presented in Figure 7d represent the sum of all possible methanol elimination pathways. Note that all methanol elimination reactions bear a rate-limiting TS of ~4 eV. The fact that the appearance energy of methanol elimination products is less than the calculated activation barriers and that the E_{col} dependence of its cross section somewhat resembles that of water elimination leads us to assume that the methanol elimination detected at low E_{col} is more likely produced by the secondary reactions of nascent $[9MG\cdot1MC + H]^+$ and the dissociating water ligand.

4. Conclusions

This work was built on a guided-ion beam tandem mass spectrometric study of the CID of WC-type protonated $[9MG\cdot1MC + H]^+$ base pair and its monohydrate $[9MG\cdot1MC + H]^+\cdot H_2O$ as well as the computational modeling of these reaction systems using various DFT, RI-MP2, and DLPNO-CCSD(T) theories. The experimental and theoretical results have provided insights into reaction thermodynamics and kinetics of intra-base-pair proton-transfer and base-pair dissociation. The work has confirmed non-statistical base-pair dissociation for WC-$[9MG\cdot1MC + H]^+$, wherein dissociation preferably occurs at a proton-transferred base-pair conformer than at a conventional conformer despite the fact that the conventional conformer is more stable and has lower dissociation energy than its proton-transferred counterpart. Combining with our previous findings of the non-statistical CID of deprotonated guanine–cytosine base pair and guanine–cytosine base-pair radical cation (all form WC-type base pairing), we may conclude that non-statistical dissociation is the nature of singly-charged guanine–cytosine base pairs. Singly-charged guanine–cytosine favors intra-base-pair proton transfer from the N1 site of guanine to the N3′ site of cytosine and the resulting proton-transferred conformer is able to make a large gain in entropy via a loose dissociation transition state.

Acknowledgements

This work was supported by National Science Foundation (Grant No. CHE 1856362). YS acknowledges CUNY Mina Rees Doctoral Dissertation Fellowship.

Supporting Information

Cartesian coordinates for the structures in Figures 1, 2, 5 and 8.

References

1 P. O. Löwdin, *Rev. Mod. Phys.*, 1963, **35**, 724-732, discussion 732-723.
2 J. D. Watson and F. H. C. Crick, *Nature*, 1953, **171**, 737-738.
3 K. Hildenbrand and D. Schulte-Frohlinde, *Free Radical Res. Commun.*, 1990, **11**, 195-206.
4 E. Nir, K. Kleinermanns and M. S. de Vries, *Nature (London)*, 2000, **408**, 949-950.
5 K. Kobayashi and S. Tagawa, *J. Am. Chem. Soc.*, 2003, **125**, 10213-10218.
6 A. K. Ghosh and G. B. Schuster, *J. Am. Chem. Soc.*, 2006, **128**, 4172-4173.
7 N. K. Schwalb and F. Temps, *J. Am. Chem. Soc.*, 2007, **129**, 9272-9273.
8 A. W. Parker, C. Y. Lin, M. W. George, M. Towrie and M. K. Kuimova, *J. Phys. Chem. B*, 2010, **114**, 3660-3667.
9 A. Szyperska, J. Rak, J. Leszczynski, X. Li, Y. J. Ko, H. Wang and K. H. Bowen, *ChemPhysChem*, 2010, **11**, 880-888.
10 Y. Seong, S. Y. Han, S.-C. Jo and H. B. Oh, *Mass Spectrom. Lett.*, 2011, **2**, 73-75.
11 Y. Rokhlenko, J. Cadet, N. E. Geacintov and V. Shafirovich, *J. Am. Chem. Soc.*, 2014, **136**, 5956-5962.
12 W. Lu and J. Liu, *Phys. Chem. Chem. Phys.*, 2016, **18**, 32222-32237.
13 J. Jie, K. Liu, L. Wu, H. Zhao, D. Song and H. Su, *Sci. Adv.*, 2017, **3**, e1700171.
14 L. Feketeová, B. Chan, G. N. Khairallah, V. Steinmetz, P. Maitre, L. Radom and R. A. J. O'Hair, *J. Phys. Chem. Lett.*, 2017, **8**, 3159-3165.
15 A. F. Cruz-Ortiz, M. Rossa, F. Berthias, M. Berdakin, P. Maitre and G. A. Pino, *J. Phys. Chem. Lett.*, 2017, **8**, 5501-5506.
16 Y. Sun, M. M. Moe and J. Liu, *Phys. Chem. Chem. Phys.*, 2020, **20**, 14875-14888.
17 G. P. Ford and B. Wang, *Int. J. Quantum Chem.*, 1992, **44**, 587-603.
18 A. O. Colson, B. Besler and M. D. Sevilla, *J. Phys. Chem.*, 1992, **96**, 9787-9794.
19 J. Florian and J. Leszczynski, *J. Am. Chem. Soc.*, 1996, **118**, 3010-3017.
20 M. Hutter and T. Clark, *J. Am. Chem. Soc.*, 1996, **118**, 7574-7577.
21 J. Bertran, A. Oliva, L. Rodriguez-Santiago and M. Sodupe, *J. Am. Chem. Soc.*, 1998, **120**, 8159-8167.
22 X. Li, Z. Cai and M. D. Sevilla, *J. Phys. Chem. B*, 2001, **105**, 10115-10123.
23 L. Gorb, Y. Podolyan, P. Dziekonski, W. A. Sokalski and J. Leszczynski, *J. Am. Chem. Soc.*, 2004, **126**, 10119-10129.
24 M. Noguera, M. Sodupe and J. Bertrán, *Theor. Chem. Acc.*, 2004, **112**, 318-326.
25 K. Kobayashi, R. Yamagami and S. Tagawa, *J. Phys. Chem. B*, 2008, **112**, 10752-10757.
26 J. D. Zhang, Z. Chen and H. F. Schaefer, III, *J. Phys. Chem. A*, 2008, **112**, 6217-6226.
27 A. Kumar and M. D. Sevilla, *J. Phys. Chem. B*, 2009, **113**, 11359-11361.
28 H.-Y. Chen, C.-L. Kao and S. C. N. Hsu, *J. Am. Chem. Soc.*, 2009, **131**, 15930-15938.
29 J. P. Ceron-Carrasco, A. Requena, E. A. Perpete, C. Michaux and D. Jacquemin, *J. Phys. Chem. B*, 2010, **114**, 13439-13445.
30 S. Steenken and J. Reynisson, *Phys. Chem. Chem. Phys.*, 2010, **12**, 9088-9093.

31 H.-Y. Chen, S.-W. Yeh, S. C. N. Hsu, C.-L. Kao and T.-Y. Dong, *Phys. Chem. Chem. Phys.*, 2011, **13**, 2674-2681.
32 Y. Lin, H. Wang, S. Gao and H. F. Schaefer, III, *J. Phys. Chem. B*, 2011, **115**, 11746–11756.
33 S. Xiao, L. Wang, Y. Liu, X. Lin and H. Liang, *J. Chem. Phys.*, 2012, **137**, 195101.
34 Y. Lin, H. Wang, S. Gao, R. Li and H. F. Schaefer, III, *J. Phys. Chem. B*, 2012, **116**, 8908-8915.
35 A. Gupta, H. M. Jaeger, K. R. Compaan and H. F. Schaefer, III, *J. Phys. Chem. B*, 2012, **116**, 5579-5587.
36 V. Sauri, J. P. Gobbo, J. J. Serrano-Pérez, M. Lundberg, P. B. Coto, L. Serrano-Andrés, A. C. Borin, R. Lindh, M. Merchán and D. Roca-Sanjuán, *J. Chem. Theory Comput.*, 2013, **9**, 481-496.
37 A. Kumar and M. D. Sevilla, *J. Phys. Chem. B*, 2014, **118**, 5453-5458.
38 Y. Lin, H. Wang, Y. Wu, S. Gao and H. F. Schaefer, III, *Phys. Chem. Chem. Phys.*, 2014, **16**, 6717-6725.
39 J. Gu, J. Wang and J. Leszczynski, *J. Phys. Chem. B*, 2015, **119**, 2454-2458.
40 J. Liu, *Phys. Chem. Chem. Phys.*, 2017, **19**, 30616-30626.
41 J. Jun and S. Y. Han, *Theor. Chem. Acc.*, 2017, **136**, 1-10.
42 E. E. Romero and F. E. Hernandez, *Phys. Chem. Chem. Phys.*, 2018, **20**, 1198-1209.
43 A. A. Arabi and C. F. Matta, *J. Phys. Chem. B*, 2018, **122**, 8631-8641.
44 Y. Han and D. Li, *J. Mol. Model*, 2019, **25**, 40.
45 L.-Y. Fu, G.-Z. Wang, B.-G. Ma and H.-Y. Zhang, *Biochem. Biophys. Res. Commun.*, 2011, **409**, 367-371.
46 W. Lu, Y. Sun, M. Tsai, W. Zhou and J. Liu, *ChemPhysChem*, 2018, **19**, 2645-2654.
47 K. Kawai, Y. Osakada and T. Majima, *ChemPhysChem*, 2009, **10**, 1766-1769.
48 Q. Gu and D. T. Haynie, *Annu. Rev. Nano Res.*, 2008, **2**, 217-285.
49 S. Y. Han, S. H. Lee, J. Chung and H. B. Oh, *J. Chem. Phys.*, 2007, **127**, 245102.
50 J. J. Park, C. S. Lee and S. Y. Han, *J. Am. Soc. Mass Spectrom.*, 2018, **29**, 2368-2379.
51 K. Hoogsteen, *Acta Crystallographica*, 1963, **16**, 907-916.
52 C. Colominas, F. J. Luque and M. Orozco, *J. Am. Chem. Soc.*, 1996, **118**, 6811-6821.
53 Y. M. Petrenko, *Biophysics (Engl. Transl.)*, 2015, **60**, 701-707.
54 R. Cheng, J. Martens and T. D. Fridgen, *Phys. Chem. Chem. Phys.*, 2020, **22**, 11546-11557.
55 J. J. Park and S. Y. Han, *J. Am. Soc. Mass Spectrom.*, 2019, **30**, 846-854.
56 Y. Fang and J. Liu, *J. Phys. Chem. A*, 2009, **113**, 11250-11261.
57 C. Rebick and R. D. Levine, *J. Chem. Phys.*, 1973, **58**, 3942-3952.
58 R. D. Levine and R. B. Bernstein, *Molecular Reaction Dynamics and Chemical Reactivity*, Oxford University Press, New York, 1987.
59 P. B. Armentrout, *Int. J. Mass Spectrom.*, 2000, **200**, 219-241.
60 J. Liu, B. van Devener and S. L. Anderson, *J. Chem. Phys.*, 2002, **116**, 5530-5543.
61 M. B. Sowa-Resat, P. A. Hintz and S. L. Anderson, *J. Phys. Chem.*, 1995, **99**, 10736-10741.
62 M. T. Rodgers, K. M. Ervin and P. B. Armentrout, *J. Chem. Phys.*, 1997, **106**, 4499-4508.
63 R. A. Marcus, *J. Chem. Phys.*, 1952, **20**, 359-364.
64 M. J. Frisch, G. W. Trucks, H. B. Schlegel, G. E. Scuseria, M. A. Robb, J. R. Cheeseman, G. Scalmani, V. Barone, B. Mennucci, G. A. Petersson, H. Nakatsuji, M. Caricato, X. Li, H. P. Hratchian, A. F. Izmaylov, J. Bloino, G. Zheng, J. L. Sonnenberg, M. Hada, M. Ehara, K. Toyota, R. Fukuda, J. Hasegawa, M. Ishida, T. Nakajima, Y. Honda, O. Kitao, H. Nakai, T. Vreven, J. J. A. Montgomery, J. E. Peralta, F. Ogliaro, M. Bearpark, J. J. Heyd, E. Brothers, K. N. Kudin, V. N. Staroverov, T. Keith, R. Kobayashi, J. Normand, K. Raghavachari, A. Rendell, J. C. Burant, S. S. Iyengar, J. Tomasi, M. Cossi, N. Rega, J. M. Millam, M. Klene, J. E. Knox, J. B. Cross, V. Bakken, C. Adamo, J. Jaramillo, R. Gomperts, R. E. Stratmann, O. Yazyev, A. J. Austin, R. Cammi, C. Pomelli, J. W. Ochterski, R. L. Martin, K. Morokuma, V. G. Zakrzewski, G. A. Voth, P. Salvador, J. J. Dannenberg, S. Dapprich, A. D. Daniels, O. Farkas, J. B. Foresman, J. V. Ortiz, J. Cioslowski and D. J. Fox, Gaussian 09, Rev. D.01, Gaussian, Inc, Wallingford, CT, 2013.
65 J.-D. Chai and M. Head-Gordon, *Phys. Chem. Chem. Phys.*, 2008, **10**, 6615-6620.

66 F. B. van Duijneveldt, J. G. C. M. van Duijneveldt-van de Rijdt and J. H. van Lenthe, *Chem. Rev.*, 1994, **94**, 1873-1885.
67 H. Wang, J. D. Zhang and H. F. Schaefer, III, *ChemPhysChem*, 2010, **11**, 622-629.
68 F. Weigend, M. Haser, H. Patzelt and R. Ahlrichs, *Chem. Phys. Lett.*, 1998, **294**, 143-152.
69 P. Jurecka, P. Nachtigall and P. Hobza, *Phys. Chem. Chem. Phys.*, 2001, **3**, 4578-4582.
70 D. G. Liakos, M. Sparta, M. K. Kesharwani, J. M. L. Martin and F. Neese, *J. Chem. Theory Comput.*, 2015, **11**, 1525-1539.
71 F. Neese, *WIREs Comput Mol Sci*, 2018, **8**, e1327.
72 I. M. Alecu, J. Zheng, Y. Zhao and D. G. Truhlar, *J. Chem. Theory Comput.*, 2010, **6**, 2872-2887.
73 T. Baer and W. L. Hase, *Unimolecular reaction dynamics: Theory and experiments*, Oxford University Press, New York, 1996.
74 W. L. Hase, *Acc. Chem. Res.*, 1998, **31**, 659-665.
75 K. Fukui, *J. Phys. Chem.*, 1970, **74**, 461-463.
76 L. Zhu and W. L. Hase, *Chem. Phys. Lett.*, 1990, **175**, 117-124.
77 L. Zhu and W. L. Hase, A General RRKM Program (QCPE 644), Quantum Chemistry Program Exchange, Chemistry Department, University of Indiana, Bloomington, 1993.
78 J. J. Dannenberg and M. Tomasz, *J. Am. Chem. Soc.*, 2000, **122**, 2062-2068.
79 L. Zendlova, P. Hobza and M. Kabelac, *ChemPhysChem*, 2006, **7**, 439-447.
80 S.-h. Urashima, H. Asami, M. Ohba and H. Saigusa, *J. Phys. Chem. A*, 2010, **114**, 11231-11237.
81 F. Meyer, F. A. Khan and P. B. Armentrout, *J. Am. Chem. Soc.*, 1995, **117**, 9740-9748.
82 M. B. More, E. D. Glendening, D. Ray, D. Feller and P. B. Armentrout, *J. Phys. Chem.*, 1996, **100**, 1605-1614.
83 D. Ray, D. Feller, M. B. More, E. D. Glendening and P. B. Armentrout, *J. Phys. Chem.*, 1996, **100**, 16116-16125.
84 M. T. Rodgers and P. B. Armentrout, *J. Chem. Phys.*, 1998, **109**, 1787-1800.
85 S. J. Klippenstein, A. L. L. East and W. D. Allen, *J. Chem. Phys.*, 1994, **101**, 9198-9201.
86 J. K. Laerdahl and E. Uggerud, *Int. J. Mass Spectrom.*, 2002, **214**, 277-314.
87 E. Uggerud, *Pure Appl. Chem.*, 2009, **81**, 709-717.

Table 1 Comparison of reaction ΔHs (298 K, eV) of WC-[9MG + H_{N7}]$^+$·1MC at different levels of theory

Species	ωB97XD/ 6-311++G(d,p)	ωB97XD/ aug-cc-pVQZ	B3LYP/ aug-cc-pVQZ	RI-MP2/ aug-cc-pVTZ	DLPNO-CCSD(T)/ aug-cc-pVTZ
WC-[9MG + H_{N7}]$^+$·1MC	0.00	0.00	0.00	0.00	0.00
[9MG + H_{N7}]$^+$ + 1MC	1.70	1.62	1.45	1.70	1.65
WC-TS_PT1	0.18	0.20	0.18	0.12	0.18
WC-[9MG + H_{N7} – H_{N1}]·[1MC + $H_{N3'}$]$^+$	0.17	0.17	0.16	0.14	0.16
WC-[9MG + H_{N7} – H_{N1}] + [1MC + $H_{N3'}$]$^+$	2.55	2.48	2.27	2.51	2.50
WC-TS_enol	1.68	1.69	1.65	1.54	1.64
WC-[9MG + H_{O6}]$^+$·1MC	0.38	0.37	0.37	0.33	0.28
[9MG + H_{O6}]$^+$ + 1MC	2.04	1.94	1.76	2.00	1.90
WC-TS_enol_PT1	0.45	0.48	0.49	0.33	0.35
WC-[9MG + H_{O6} – H_{N1}]·[1MC + $H_{N3'}$]$^+$	0.42	0.44	0.45	0.35	0.33
[9MG + H_{O6} – H_{N1}] + [1MC + $H_{N3'}$]$^+$	1.83	1.75	1.59	1.76	1.70

Table 2 Comparison of reaction ΔHs (298 K, eV) of WC-[9MG + H_{N7}]$^+$·1MC·H_2O at different levels of theory

Species	ωB97XD/ 6-311++G(d,p)	ωB97XD/ aug-cc-pVQZ	B3LYP/ aug-cc-pVQZ	RI-MP2/ aug-cc-pVTZ	DLPNO-CCSD(T)/ aug-cc-pVTZ
WC-[9MG + H_{N7}]$^+$·1MC·H_2O	0.00	0.00	0.00	0.00	0.00
WC-[9MG + H_{N7}]$^+$·1MC + H_2O	0.69	0.61	0.54	0.65	0.62
[9MG + H_{N7}]$^+$ + 1MC + H_2O	2.39	2.23	1.99	2.35	2.27
WC-TS_PT1·H_2O	0.18	0.20	0.20	0.11	0.17
WC-[9MG + H_{N7} – H_{N1}]·[1MC + $H_{N3'}$]$^+$·H_2O	0.19	0.20	0.19	0.15	0.18
WC-[9MG + H_{N7} – H_{N1}]·[1MC + $H_{N3'}$]$^+$ + H_2O	0.86	0.79	0.70	0.79	0.78
[9MG + H_{N7} – H_{N1}] + [1MC + $H_{N3'}$]$^+$ + H_2O	3.24	3.10	2.81	3.16	3.12
WC-TS_enol·H_2O	0.31	0.30	0.28	0.21	0.28
WC-[9MG + H_{O6}]$^+$·1MC·H_2O	0.22	0.21	0.21	0.18	0.14
[9MG + H_{O6}]$^+$·1MC + H_2O	1.07	0.99	0.91	0.99	0.90
[9MG + H_{O6}]$^+$ + 1MC + H_2O	2.73	2.56	2.30	2.65	2.52
WC-TS_PT1_enol·H_2O	0.32	0.35	0.36	0.21	0.24
WC-[9MG + H_{O6} – H_{N1}]·[1MC + $H_{N3'}$]$^+$·H_2O	0.32	0.33	0.34	0.24	0.25
WC-[9MG + H_{O6} – H_{N1}]·[1MC + $H_{N3'}$]$^+$ + H_2O	1.11	1.06	0.99	1.00	0.95
[9MG + H_{O6} – H_{N1}] + [1MC + $H_{N3'}$]$^+$ + H_2O	2.52	2.36	2.13	2.41	2.33
WC-TS1	4.08	4.14	3.86	4.24	4.14
WC-[9MG + H_{N7}]$^+$·1HC + CH_3OH	1.17	1.08	0.92	1.29	1.16
[9MG + H_{N7}]$^+$ + 1HC + CH_3OH	2.83	2.66	2.34	2.95	2.77
WC-TS1_PT1	1.36	1.29	1.12	1.42	1.35
WC-[9MG + H_{N7} – H_{N1}]·[1HC + $H_{N3'}$]$^+$ + CH_3OH	1.36	1.28	1.11	1.44	1.34
[9MG + H_{N7} – H_{N1}] + [1HC + $H_{N3'}$]$^+$ + CH_3OH	3.83	3.67	3.31	3.90	3.76
WC_TS2	3.72	3.78	3.58	3.89	3.77
WC-[9HG + H_{N7}]$^+$·1MC + CH_3OH	1.33	1.23	1.08	1.43	1.30
[9HG + H_{N7}]$^+$ + 1MC + CH_3OH	3.05	2.87	2.55	3.16	2.97
WC_TS2_PT1	1.49	1.41	1.25	1.54	1.46
WC-[9HG + H_{N7} – H_{N1}]·[1MC + $H_{N3'}$]$^+$ + CH_3OH	1.48	1.38	1.21	1.54	1.44
[9HG + H_{N7} – H_{N1}] + [1MC + $H_{N3'}$]$^+$ + CH_3OH	3.80	3.63	3.26	3.86	3.72

Scheme 1 Watson-Crick and Hoogsteen base-pair structures of $[9MG{\cdot}1MC + H]^+$, presented with atomic numbering scheme and possible intra-base-pair PT and HT pathways

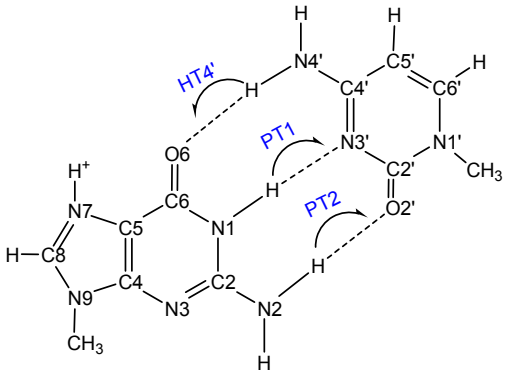

WC-$[9MG{\cdot}1MC + H]^+$

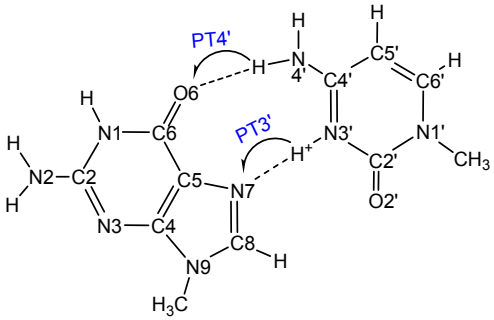

Hoo-$[9MG{\cdot}1MC + H]^+$

Figure Caption

Fig. 1 Stable conformers of WC-[9MG·1MC + H]$^+$. Dashed lines indicate H-bonds. Relative formation enthalpies (ΔH at 298 K with respect to the global minimum, unit eV) were calculated at the ωB97XD/6-311++G(d,p) level of theory, including thermal corrections.

Fig. 2 Stable conformers of monohydrated WC-[9MG·1MC + H]$^+$·H_2O. Dashed lines indicate H-bonds. Relative formation enthalpies (ΔH at 298 K with respect to the global minimum, unit eV) and hydration enthalpies ($\Delta H_{hydration}$, eV) were calculated at the ωB97XD/6-311++G(d,p) level of theory, including thermal corrections.

Fig. 3 (a) CID product ion mass spectrum of WC-[9MG + H_{N7}]$^+$·1MC with Xe measured at E_{col} = 3.0 eV; and (b, c) cross sections of product ions [9MG + H]$^+$ and [1MC+ H]$^+$ as a function of E_{col}, where the circled points are experimental data and the solid lines are LOC fits as described in the text.

Fig. 4 Comparison of E_{col}-dependent product ion branching ratios for (a) WC-[9MG·1MC + H]$^+$, (b) [9MG·1MC]$^{\bullet+}$ and (c) [9MG·C – H]$^-$, where circled points are experimental data and solid curves are RRKM fits as discussed in the text.

Fig. 5 PES for intra-base-pair PT and dissociation of WC-[9MG + H_{N7}]$^+$·1MC. Reaction ΔHs were calculated at DLPNO-CCSD(T)/aug-cc-PVTZ//ωB97XD/6-311++G(d,p), including thermal corrections at 298 K.

Fig. 6 CID product ion mass spectrum of WC-[9MG + H_{N7}]$^+$·1MC·H_2O with Xe measured at E_{col} = 3.0 eV.

Fig. 7 (a – d) Individual product ion cross sections for the CID of WC-[9MG + H_{N7}]$^+$·1MC·H_2O with Xe; and (e) product ion branching ratio of [1MC + H]$^+$/[9MG + H]$^+$.

Fig. 8 PES for intra-base-pair reactions and dissociation of WC-[9MG + H_{N7}]$^+$·1MC·H_2O. Reaction ΔHs were calculated at DLPNO-CCSD(T)/aug-cc-PVTZ//ωB97XD/6-311++G(d,p), including thermal corrections at 298 K.

Fig. 1

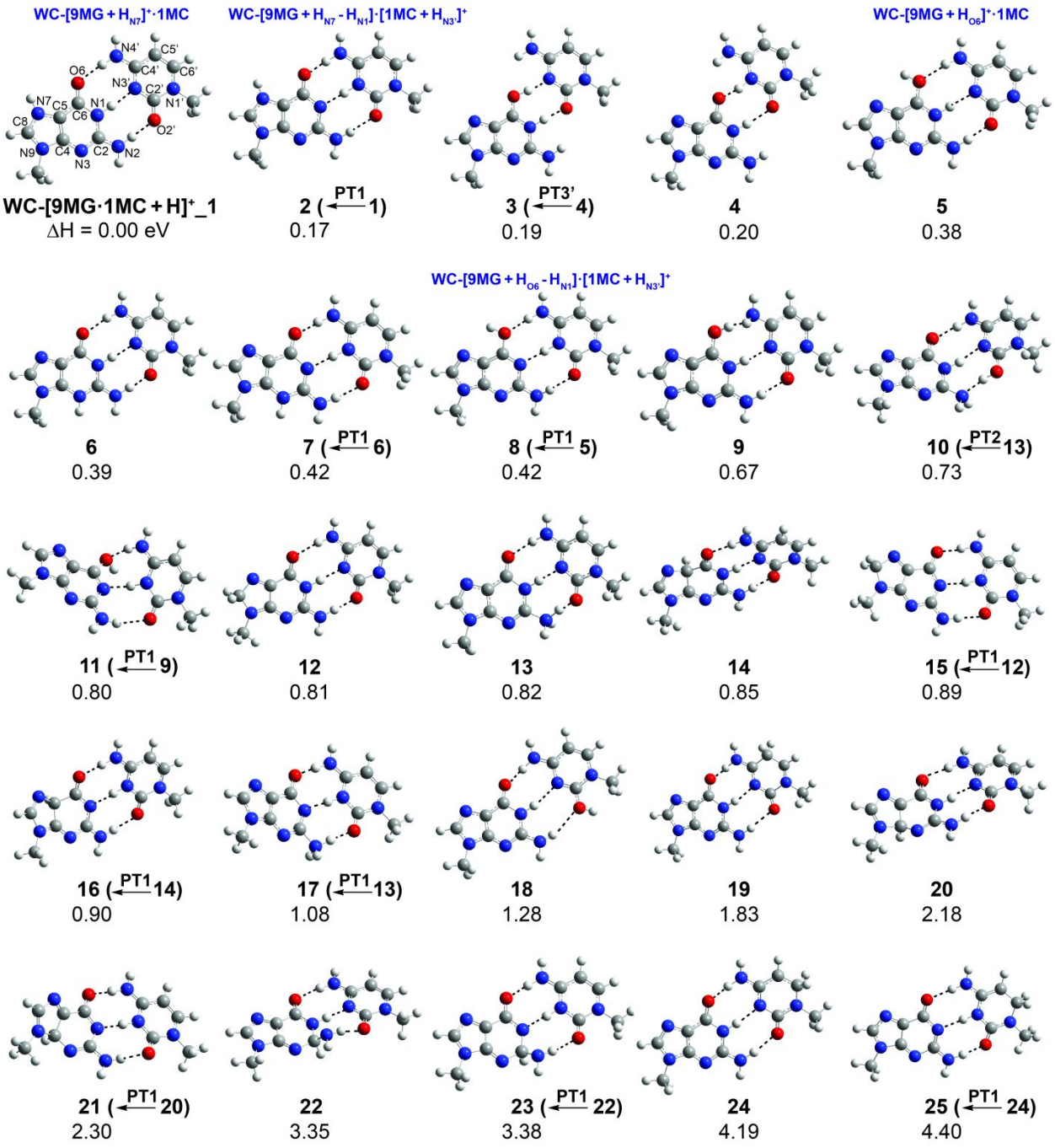
WC-[9MG + H$_{N7}$]$^{+}$·1MC
WC-[9MG + H$_{N7}$ - H$_{N1}$]·[1MC + H$_{N3'}$]$^{+}$
WC-[9MG + H$_{O6}$]$^{+}$·1MC
WC-[9MG·1MC + H]$^{+}$_1
ΔH = 0.00 eV
2 (PT1 1)
0.17
3 (PT3' 4)
0.19
4
0.20
5
0.38
WC-[9MG + H$_{O6}$ - H$_{N1}$]·[1MC + H$_{N3'}$]$^{+}$
6
0.39
7 (PT1 6)
0.42
8 (PT1 5)
0.42
9
0.67
10 (PT2 13)
0.73
11 (PT1 9)
0.80
12
0.81
13
0.82
14
0.85
15 (PT1 12)
0.89
16 (PT1 14)
0.90
17 (PT1 13)
1.08
18
1.28
19
1.83
20
2.18
21 (PT1 20)
2.30
22
3.35
23 (PT1 22)
3.38
24
4.19
25 (PT1 24)
4.40

Fig. 2

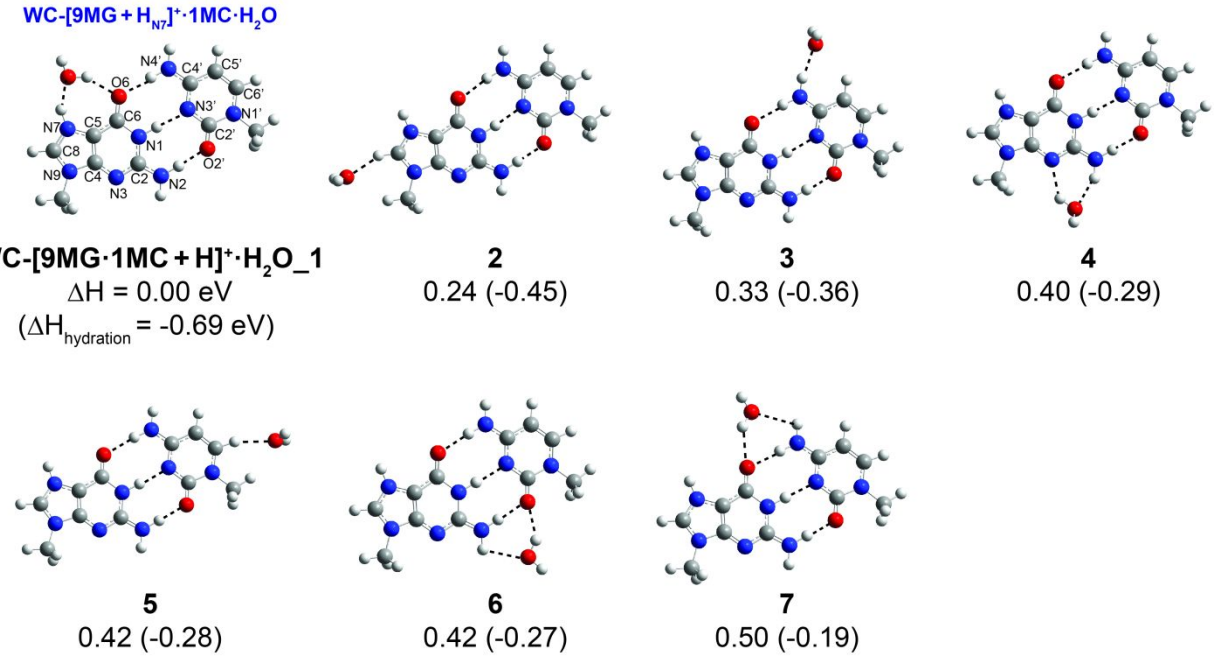
WC-[9MG + H$_{N7}$]$^{+}$·1MC·H$_2$O
N4'
C4'
C5'
O6
C6'
N3'
N1'
N7
C5
C6
C2'
C8
N1
O2'
N9
C4
C2
N2
N3
WC-[9MG·1MC + H]$^{+}$·H$_2$O_1
ΔH = 0.00 eV
(ΔH$_{hydration}$ = -0.69 eV)
2
0.24 (-0.45)
3
0.33 (-0.36)
4
0.40 (-0.29)
5
0.42 (-0.28)
6
0.42 (-0.27)
7
0.50 (-0.19)

Fig. 3

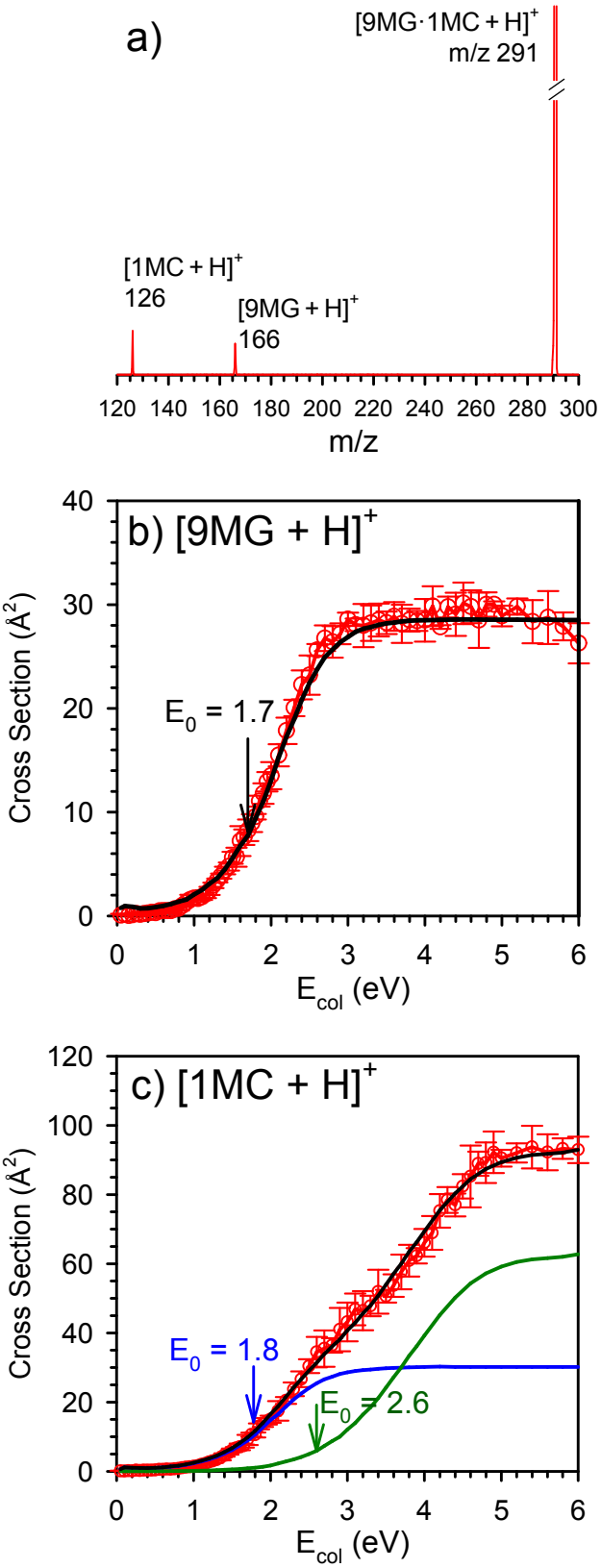
a)
[9MG·1MC + H]+
m/z 291
[1MC + H]+
126
[9MG + H]+
166
120 140 160 180 200 220 240 260 280 300
m/z
b) [9MG + H]+
E0 = 1.7
Cross Section (Å2)
Ecol (eV)
c) [1MC + H]+
E0 = 1.8
E0 = 2.6
Cross Section (Å2)
Ecol (eV)

Fig. 4

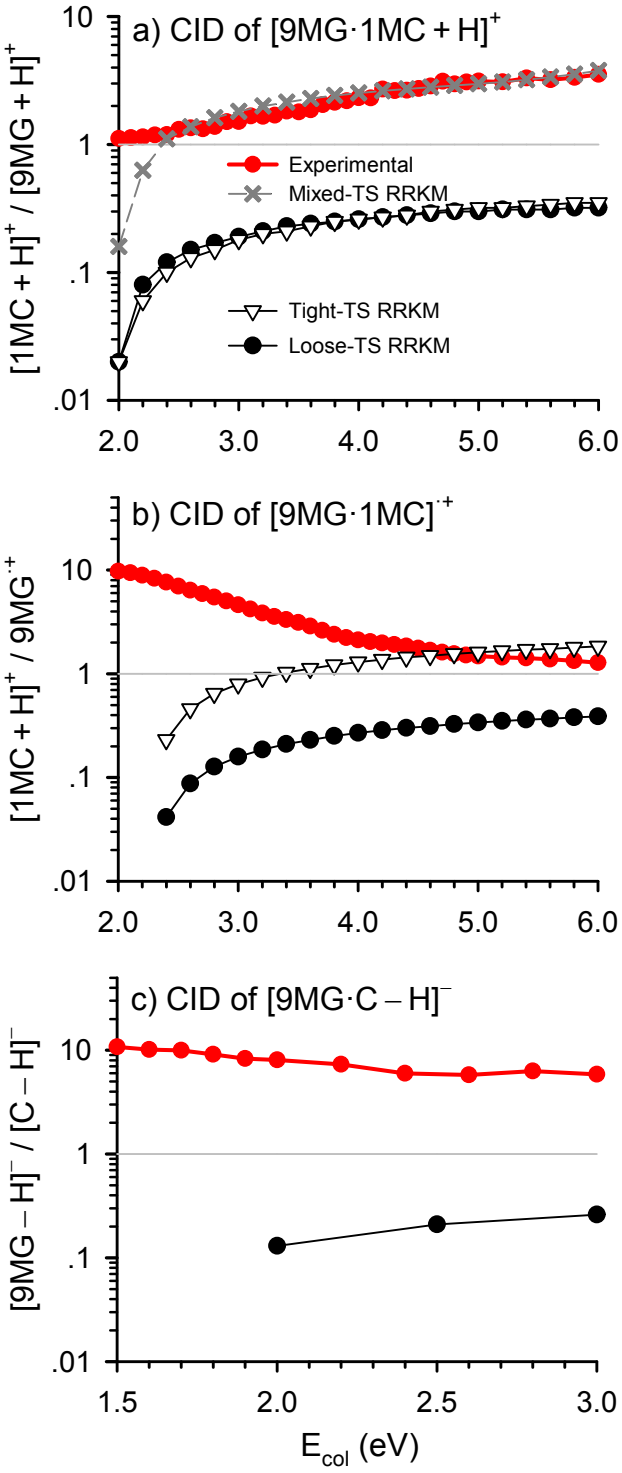
a) CID of [9MG·1MC + H]+
[1MC + H]+ / [9MG + H]+
Experimental
Mixed-TS RRKM
Tight-TS RRKM
Loose-TS RRKM
b) CID of [9MG·1MC]·+
[1MC + H]+ / 9MG·+
c) CID of [9MG·C – H]–
[9MG – H]– / [C – H]–
Ecol (eV)

Fig. 5

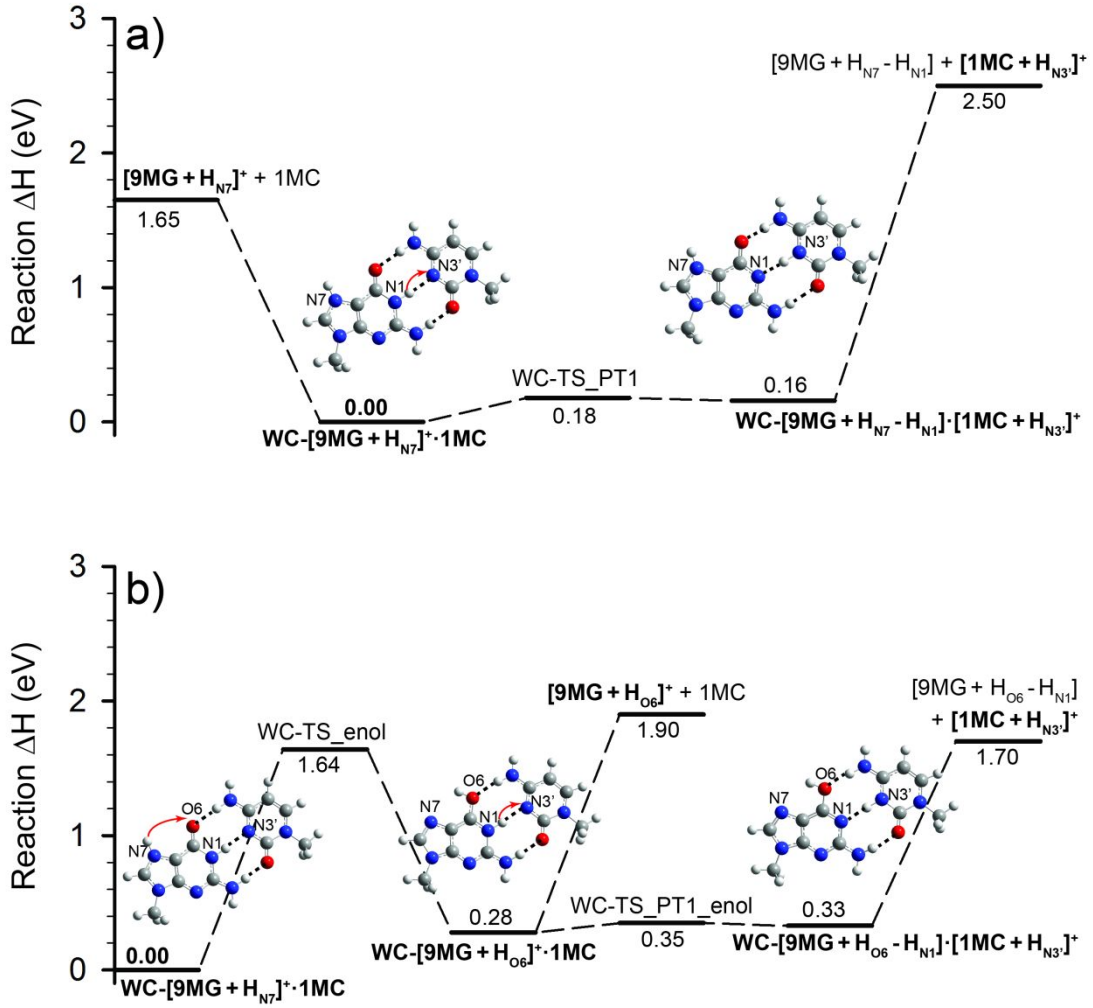
a)
Reaction ΔH (eV)
[9MG + H$_{N7}$]$^+$ + 1MC
1.65
0.00
WC-[9MG + H$_{N7}$]$^+$·1MC
WC-TS_PT1
0.18
0.16
WC-[9MG + H$_{N7}$ - H$_{N1}$]·[1MC + H$_{N3'}$]$^+$
[9MG + H$_{N7}$ - H$_{N1}$] + [1MC + H$_{N3'}$]$^+$
2.50
b)
Reaction ΔH (eV)
WC-TS_enol
1.64
0.00
WC-[9MG + H$_{N7}$]$^+$·1MC
[9MG + H$_{O6}$]$^+$ + 1MC
1.90
0.28
WC-[9MG + H$_{O6}$]$^+$·1MC
WC-TS_PT1_enol
0.35
0.33
WC-[9MG + H$_{O6}$ - H$_{N1}$]·[1MC + H$_{N3'}$]$^+$
[9MG + H$_{O6}$ - H$_{N1}$]
+ [1MC + H$_{N3'}$]$^+$
1.70

Fig. 6

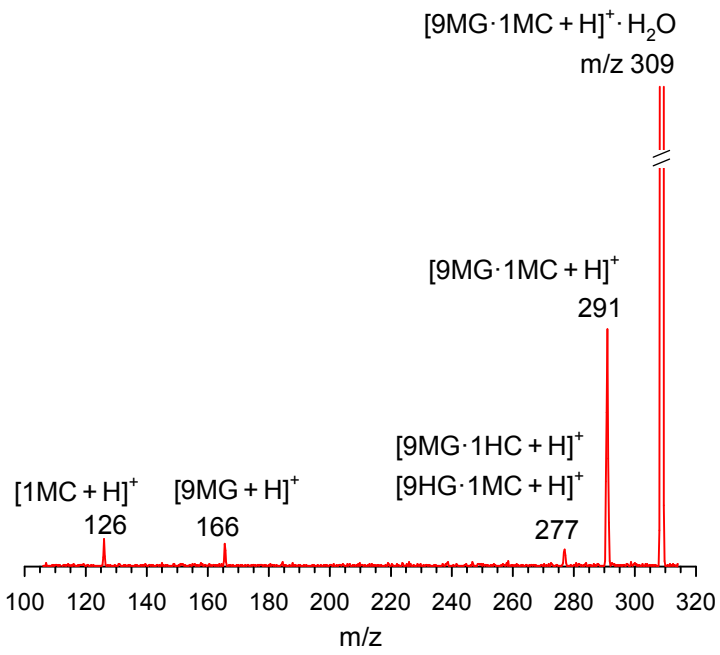
[9MG·1MC + H]+· H2O
m/z 309
[9MG·1MC + H]+
291
[9MG·1HC + H]+
[9HG·1MC + H]+
277
[1MC + H]+
126
[9MG + H]+
166
100 120 140 160 180 200 220 240 260 280 300 320
m/z

Fig. 7

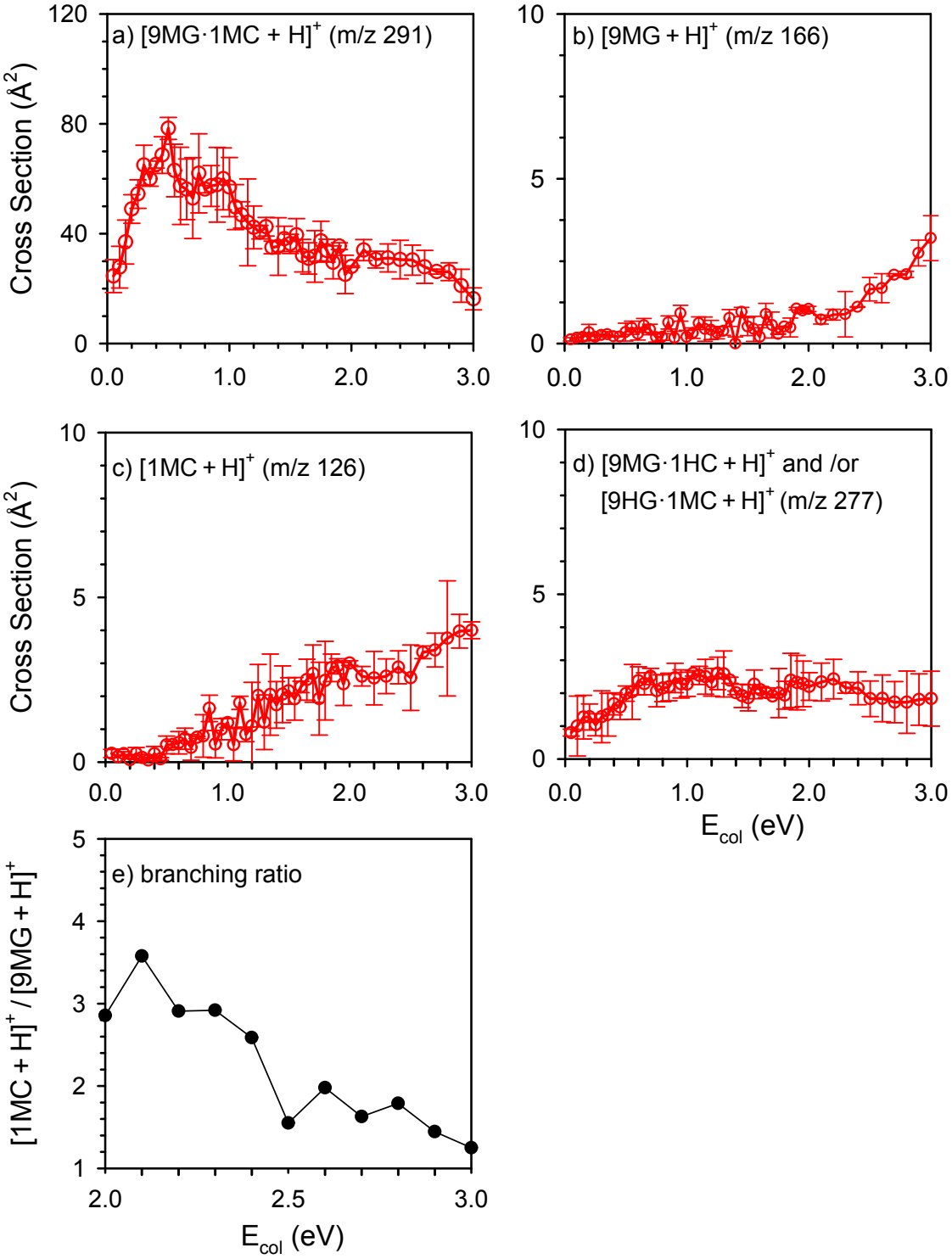
a) [9MG·1MC + H]+ (m/z 291)
b) [9MG + H]+ (m/z 166)
c) [1MC + H]+ (m/z 126)
d) [9MG·1HC + H]+ and /or
[9HG·1MC + H]+ (m/z 277)
e) branching ratio
Cross Section (Å2)
[1MC + H]+ / [9MG + H]+
Ecol (eV)

Fig. 8

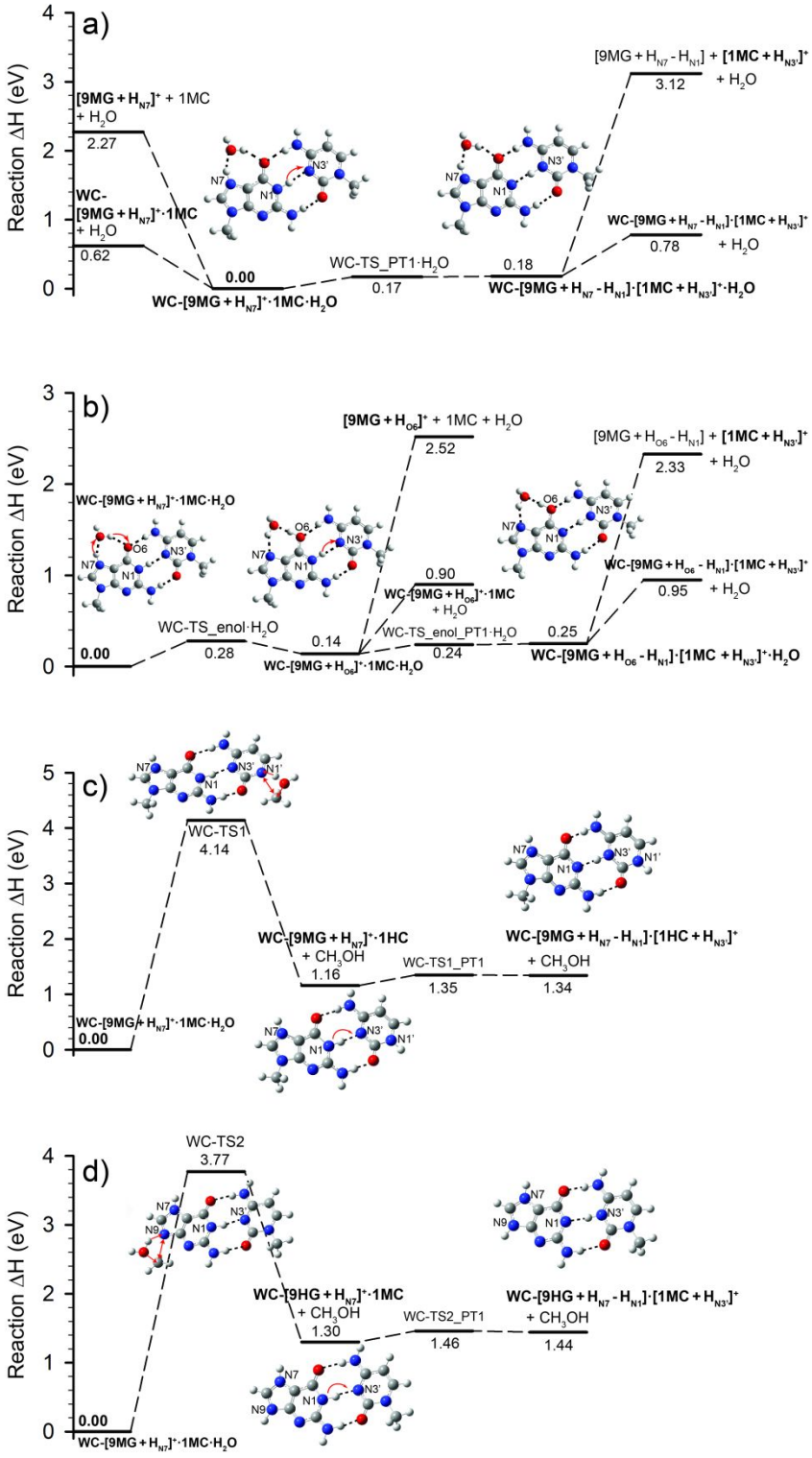
a)
Reaction ΔH (eV)
[9MG + H_N7]+ + 1MC + H2O
2.27
WC-[9MG + H_N7]+·1MC + H2O
0.62
0.00
WC-[9MG + H_N7]+·1MC·H2O
WC-TS_PT1·H2O
0.17
0.18
[9MG + H_N7 - H_N1] + [1MC + H_N3']+ + H2O
3.12
WC-[9MG + H_N7 - H_N1]·[1MC + H_N3']+ + H2O
0.78
WC-[9MG + H_N7 - H_N1]·[1MC + H_N3']+·H2O
b)
Reaction ΔH (eV)
WC-[9MG + H_N7]+·1MC·H2O
0.00
WC-TS_enol·H2O
0.28
0.14
WC-[9MG + H_O6]+·1MC·H2O
[9MG + H_O6]+ + 1MC + H2O
2.52
0.90
WC-[9MG + H_O6]+·1MC + H2O
WC-TS_enol_PT1·H2O
0.24
0.25
[9MG + H_O6 - H_N1] + [1MC + H_N3']+ + H2O
2.33
WC-[9MG + H_O6 - H_N1]·[1MC + H_N3']+ + H2O
0.95
WC-[9MG + H_O6 - H_N1]·[1MC + H_N3']+·H2O
c)
Reaction ΔH (eV)
WC-[9MG + H_N7]+·1MC·H2O
0.00
WC-TS1
4.14
WC-[9MG + H_N7]+·1HC + CH3OH
1.16
WC-TS1_PT1
1.35
WC-[9MG + H_N7 - H_N1]·[1HC + H_N3']+ + CH3OH
1.34
d)
Reaction ΔH (eV)
WC-[9MG + H_N7]+·1MC·H2O
0.00
WC-TS2
3.77
WC-[9HG + H_N7]+·1MC + CH3OH
1.30
WC-TS2_PT1
1.46
WC-[9HG + H_N7 - H_N1]·[1MC + H_N3']+ + CH3OH
1.44

Graphic for TOC

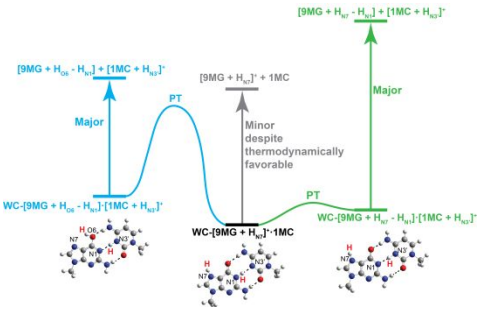

Non-statistical dissociation of protonated guanine-cytosine Waterson-Crick base pair